MIT Open Access Articles

Condensation on Superhydrophobic Copper Oxide Nanostructures

Massachusetts Institute of Technology

Condensation on superhydrophobic copper oxide nanostructures

Ryan Enright[1,2,*]*, Nenad Miljkovic*[1]*, Nicholas Dou*[1]*, Youngsuk Nam*[1,3]*, and Evelyn N. Wang*[1]

[1]Department of Mechanical Engineering, Massachusetts Institute of Technology, 77 Massachusetts Avenue, Cambridge, Massachusetts, 02139, USA

[2]Stokes Institute, University of Limerick, Limerick, Ireland

[3]Kyung Hee University, Yongin, Korea

*Current address: Thermal Management and Eco-sustainability Research Group, Bell Labs Ireland, Alcatel-Lucent, Blanchardstown Business & Technology Park, Snugborough Rd, Dublin 15, Ireland

Corresponding authors: ryan.enright@alcatel-lucent.com, enwang@mit.edu

ABSTRACT

Condensation is an important process in both emerging and traditional power generation and water desalination technologies. Superhydrophobic nanostructures promise enhanced condensation heat transfer by reducing the characteristic size of departing droplets *via* coalescence-induced shedding. In this work, we investigated a scalable synthesis technique to produce functionalized oxide nanostructures on copper surfaces capable of sustaining superhydrophobic condensation and characterized the growth and departure behavior of the condensed droplets. Nanostructured copper oxide (CuO) films were formed *via* chemical oxidation in an alkaline solution resulting in dense arrays of sharp CuO nanostructures with characteristic heights and widths of ~1 μm and ~300 nm, respectively. To make the CuO surfaces superhydrophobic, they were functionalized by direct deposition of a fluorinated silane molecular film or by sputtering a thin gold film before depositing a fluorinated thiol molecular film. Condensation on these surfaces was characterized using optical microscopy and environmental scanning electron microscopy to quantify the distribution of nucleation sites and elucidate the growth behavior of individual droplets with characteristic radii of ~1 to 10 μm at supersaturations $\leq$ 1.5. Comparison of the measured individual droplet growth behavior to our developed heat transfer model for condensation on superhydrophobic surfaces showed good agreement. Prediction of the overall heat transfer enhancement in comparison to a typical dropwise condensing surface having an identical nucleation density suggests a restricted regime of enhancement limited to droplet shedding radii $\lesssim$ 2.5 μm due to the large apparent contact angles of

condensed droplets on the fabricated CuO surfaces. The findings demonstrate that superhydrophobic condensation typified by coalescence-induced droplet shedding may not necessarily enhance heat transfer and highlights the need for further quantification of the effects of surface structure on nucleation density and careful surface design to minimize parasitic thermal resistances.

Keywords: condensation, superhydrophobic, nanostructure, scalable synthesis, heat transfer, droplet jumping, experimental, modeling

INTRODUCTION

The utilization of superhydrophobic surfaces is of particular interest as a means to improve the efficiency of heat and mass transport processes dependent on the condensation of water such as power generation [1], water desalination [2], and environmental control [3]. By promoting the formation of weakly-pinning droplet morphologies, coalescence-induced droplet shedding can significantly reduce the average droplet size on the surface, which promises to enhance condensation heat and mass transfer rates beyond those obtained using gravity-driven droplet removal on smooth dropwise condensing surfaces [4, 5]. However, in order to apply these surfaces in large-scale applications, there is a need to develop scalable processes compatible with existing engineering heat transfer materials such as copper that can promote desired wetting behavior during condensation. Furthermore, the synthesis method should minimize parasitic thermal resistances that could negate the advantage of this unique wetting behavior. Indeed, while recent experimental studies have explored droplet wetting-states formed during condensation on structured surfaces fabricated *via* scalable synthesis methods [6-13], the measurement of individual droplet heat transfer rates obtained from detailed growth studies and overall heat transfer measurements are required to validate the efficacy of a particular surface structuring technique. This is due to the fact that coalescence-induced droplet shedding does not necessarily imply enhanced heat transfer due to the important nature of the thermal resistances comprising an individual droplet system [4], i.e., the details of the local wetting state beneath the droplet and the structure geometry such as the roughness height.

Superhydrophobic condensation can be achieved provided that the structured surface satisfies a scale-invariant wetting energy criterion determined by the details of the structure geometry and a structure length-scale requirement controlled by the nucleation density [14]. The scale-invariant wetting energy criterion determines whether the contact line of an individual droplet remains pinned at the base of a partially-wetting droplet, leading to a weakly-pinned Cassie-like

state [15], or de-pins, completely wetting the surface structures to form a Wenzel droplet [16]. The pinning energy barrier during growth is estimated from the *non-equilibrium* Wenzel equation, $\cos\theta_a^W = r\cos\theta_a$, where the surface roughness r is defined by the area ratio of the rough surface in comparison to a corresponding smooth surface (projected area) and θ_a is the advancing contact angle associated with the hydrophobic coating. For the case of a structured surface with unconnected roughness elements, i.e., pillars, this pinning barrier is then compared to the pinning barrier associated with the droplet advancing over the structured surface in the Cassie state, $\cos\theta_a^{CB} = -1$ [17], giving the following expression

$$E^* = \frac{\cos\theta_a^{CB}}{\cos\theta_a^W} = \frac{-1}{r\cos\theta_a}. \tag{1}$$

When $E^* > 1$, the contact line located within the structured region can overcome the energy barrier to de-pin and a Wenzel drop is formed. If $E^* < 1$, complete de-pinning is prevented and the droplet spreads over the top of the structured region forming a Cassie-like droplet as the drop radius, R, becomes larger than a length scale characterizing the pinning barrier, $R \gg l$. Equation (1) represents a simplification of contact line pinning behavior and has been shown to underestimate the transition from Cassie to Wenzel droplet growth on model surfaces composed of well-defined pillar structures. This result is due to the fact that the pinning barrier preventing Wenzel droplet growth is typically larger than that defined simply by the surface roughness, r, due to complexities in the local contact line behavior [14]. A further subtlety not captured by Eq. (1) arises when considering surfaces that have a non-uniform structure height across the surface. This non-uniformity can allow the interface of a growing droplet to make contact with the surrounding surface for apparent contact angles less than 180°, implying that $\cos\theta_a^{CB} > -1$. These two effects complement each other to improve the stability of the partially-wetting Cassie state such that Eq. (1) represents a conservative estimate of the preferred wetting state during droplet growth in the absence of interactions with other droplets.

The second criterion for superhydrophobic condensation is defined by a scale requirement that links the characteristic spacing of the roughness defining the pinning energy barrier, l, to the mean separation distance between nucleation sites, $\langle L \rangle$. For stable Cassie growth, $\langle L \rangle / l \gtrsim 2$ is the minimum requirement to avoid by-passing the pinning barrier defined by the denominator in Eq. (1) during droplet coalescence [14]. If this geometric scale criterion is not met, the Wenzel state emerges during condensation regardless of the preferred wetting state predicted by Eq. (1). Thus, this implies a general requirement for the nucleation density to be less than the density of the surface structures, $N < l^{-2}$, for the Cassie state to emerge.

Here we demonstrate a scalable synthesis method for modifying copper surfaces to create oxide nanostructures that, once functionalized, can maintain Cassie condensation behavior while minimizing parasitic resistances (oxide thickness) due to the self-limiting behavior of the chemical oxidation process used. A combination of imaging and a derived wetting model is used to identify the upper limit on the nucleation density leading to the suppression of droplet jumping. Individual droplet growth measurements coupled with an overall heat transfer model indicates that there is a critical minimum nucleation density on the CuO surface that delineates heat transfer enhancement with respect to a smooth hydrophobic surface with the same nucleation density due to increased conduction resistance associated with the large droplet apparent contact angles on the CuO surface. By considering these two nucleation density limits and assuming ideal coalescence-induced droplet shedding, the maximum heat transfer enhancement is predicted to be in the range of 1 – 1.25× compared to the smooth hydrophobic surface.

SURFACE SYNTHESIS & CHARACTERIZATION

To synthesize the nanostructured surfaces, we used commercially available oxygen-free copper (Cu) sheet (99.9 % purity, 0.8 mm thickness) diced into ~1 – 2 cm^2 tabs as starting substrates. Each Cu tab was cleaned in an ultrasonic bath with acetone for ~10 min and rinsed with ethanol, isopropyl alcohol and de-ionized (DI) water. The substrates were then dipped into a 2.0 M hydrochloric acid solution for 5 min to remove the native oxide film on the surface, then triple-rinsed with DI water, and dried with in a clean nitrogen stream.

Nanostructured copper oxide films were formed by immersing the cleaned substrate into a hot (~95 ± 2°C) alkaline solution composed of NaClO$_2$, NaOH, Na$_3$PO$_4$·12H$_2$O, and DI water (3.75 : 5 : 10 : 100 wt.%). During the oxidation process, a thin and conformal Cu$_2$O layer is initially formed on the copper surface that then re-oxidizes to form sharp, spike-like CuO oxide structures. Figure 1a shows the CuO nanostructures beginning to grow from the Cu$_2$O intermediate layer. The surface reaction leading to the formation of the CuO nanostructures is described as [18]:

$$2Cu + 2OH^- \rightarrow Cu_2O + H_2O + 2e^- \tag{2}$$

$$Cu_2O + 2OH^- \rightarrow 2CuO + H_2O + 2e^- \tag{3}$$

In Eq. (2), two surface Cu atoms react with two hydroxides from the solution forming Cu$_2$O, with water and two electrons as by-products. Equation (3) shows that Cu$_2$O is subsequently converted to CuO by a further hydroxide reaction with water and two electrons as by-products.

The height of the CuO nanostructures was approximately 1 µm after ~5 minutes of growth (Figure 1b). As the density of the CuO structures increases, the oxide growth rate significantly decreases to an almost negligible level as the CuO layer passivates the copper surface by creating a diffusion barrier [19]. The results of x-ray diffraction (XRD) (Figure 1c) show a strong CuO peak originating from the sharp oxide nanostructures and a weak Cu_2O peak from the underlying layer.

To characterize the total oxide thickness of the fabricated samples, we used focused ion beam milling (FIB) (NVision 40 Dual Beam Focused Ion Beam, Carl Zeiss GMBH) and SEM imaging. Milling was performed with normal incidence of the ion beam (sample tilt of 54°), ion beam energy of 30 keV, and ion current of 300 pA. The structure cross-sections were obtained by milling 8 µm deep x 20 µm wide trenches. Due to the good milling response of Cu, surface polishing was not required. All samples were imaged at 36° tilt using the in lens detector with electron beam energies of 7 keV. Figure 1d shows the cross-section images of a nanostructured sample. The underlying Cu_2O oxide thickness was found to be $\delta_{Cu2O} \approx 300$ nm. With the addition of the CuO nanostructures, the total copper oxide thickness was $\delta_{Cu2O} + \delta_{CuO} \approx$ 1.5 µm. The morphology of the CuO nanostructures resemble thin, but broad blades converging to a sharp point with a typical thickness of ≤ 100 nm and average widths of ≈ 300 nm.

The unique blade-like morphology of the CuO nanostructures, with a tip dimension of ≲ 10 nm, ensure nucleation within the structure (as opposed to the tips of the structure) due to the increased energy barrier associated with nucleation on features similar in size to the critical nucleation radius ($R_c \leq 35$ nm for water and typical condensation conditions studied here [20]). This feature of the nanostructure geometry promotes the formation of partially-wetting droplet morphologies, which are essential to minimizing individual droplet thermal resistance, [4, 21] since Gibb's criterion can be satisfied [22, 23]. Furthermore, the self-limiting behavior of the oxidation process is critical to minimizing the parasitic thermal conduction resistance of the oxide layers since the bulk thermal conductivities of the two copper oxide species ($k_{CuO} \approx 20$ W/m.K, $k_{Cu2O} \approx 30$ W/m.K [24]) are an order of magnitude smaller than the native copper substrate ($k_{CuO} \approx 400$ W/m.K).

The CuO nanostructures were subsequently functionalized using one of two approaches. In the first approach, a ≈ 30 nm-thick coating of Au was sputtered onto the CuO nanostructures. The samples were solvent rinsed, dried and plasma cleaned before immersion into a 1 mM solution of 1H, 1H, 2H, 2H-perfluorodecanethiol (Sigma-Aldrich) in ethanol for 1

hr. Goniometric measurements (MCA-3, Kyowa Interface Science) of $\approx$ 100 nL droplets on a smooth thiolated Au surface showed advancing and receding contact angles of $\theta_a = 121.1° \pm 2.2°$ and $\theta_r = 106.3° \pm 2.4°$, respectively. In the second functionalization approach, a fluorinated silane (trichloro(1H,1H,2H,2H-perfluorooctyl)silane, Sigma-Aldrich) was deposited from a chemical vapor directly onto the oxide nanostructures. Goniometric measurements on corresponding smooth, silanated CuO surfaces showed advancing and receding contact angles of $\theta_a/\theta_r = 123.4° \pm 2.5°/81.2° \pm 8.4°$. The effective solid fraction corresponding to the surface area fraction in contact with the droplet, ϕ_{eff}, of the CuO surface was extracted from apparent contact angle measurements of a macroscopic water droplet placed onto the Au/thiol-functionalized CuO surface, $\theta_a^{CB} = 164.9° \pm 2.8° (\Delta\theta \approx 2°)$. Slightly different wetting behavior was observed for the silanated CuO surfaces with $\theta_a^{CB} = 169.2° \pm 2.6° (\Delta\theta \approx 5°)$. Using the Cassie-Baxter equation [23], $\cos\theta_a^{CB} = \varphi_{eff}(\cos\theta_a + 1) - 1$, the effective solid fraction was calculated to be $\varphi_{eff} \approx 0.071$ and $\varphi_{eff} \approx 0.039$ for the Au/thiol and silanated CuO surfaces, respectively.

In order to obtain the effective roughness defining the pinning energy barrier in Eq. 1, contact angle measurements of formamide droplets (Molecular biology grade, Sigma) were performed on both a Au/thiol-functionalized smooth and nanostructured surface. The advancing angle on the smooth surface was found to be $\theta_a = 95.3° \pm 1.4° (\theta_r = 90.2° \pm 2.1°)$, while the advancing Wenzel angle on the CuO surface was found to be $\theta_a^W = 160.6° \pm 3.2° (\theta_r^W = 145.9° \pm 2°)$. The Wenzel state was inferred through observation of significant contact angle hysteresis, $\Delta\theta \approx 15°$, in comparison to the Cassie behavior. Using the Wenzel equation, the effective roughness was calculated to be $r_{eff} = 10.2 \pm 2.8$. This effective roughness value should be viewed as a measure of the complex contact line pinning behavior on the CuO nanostructures rather than an absolute measure of the roughness [25].

OPTICAL MICROSCOPY CONDENSATION EXPERIMENTS

Global droplet nucleation and growth behavior was studied with optical microscopy using a custom built experimental set-up shown in Figure 2. Samples were mounted to a temperature-controlled stage (TS102-00, Instec). Good thermal contact between the sample and the temperature control stage was ensured by interposing a thin layer of thermal grease (Omegatherm, Omega) with a reported thermal conductivity of 2.2 W/m.K. The thermal grease was applied to the cold stage using a rigid plastic edge and progressively thinned down to $\lesssim$ 50 μm, to prevent air bubbles

being trapped in the film. The sample was then pressed down onto the film while simultaneously twisting to squeeze out excess thermal grease. Due to the low heat fluxes characteristic of the optical microscopy measurements, temperature differences between the sample and the stage were negligible. This was confirmed by mounting a 1 mm thick cooper sample with an embedded calibrated thermocouple to the stage. The temperature measured by the cold stage corresponded to the embedded thermocouple reading to within the uncertainty of the thermocouple ($\pm$0.2 K) under typical test conditions.

The mounted sample was first cooled to the test temperature by the temperature-control stage under an atmosphere of dry N_2. Once the stage temperature stabilized at the test temperature, T_w = 283$\pm$0.1 K, the by-pass valve was closed to initiate the flow of water-saturated N_2 into the top of the sample enclosure at a constant flow rate of Q = 2.5 $\pm$ 0.3 L/min (FL-2040, Omega), marking the start of the experiment. Based on the dimensions of the cylindrical enclosure (diameter = 4 cm, height = 3 cm) and the microscopic objective within the enclosure (diameter = 2 cm, height = 2.9 cm), we calculated a characteristic chamber velocity of $\approx$ 4.4x10^{-2} m/s and a characteristic fluid displacement time of $\approx$ 0.7 s. The chamber humidity was recorded throughout the experiment using a humidity probe (Hygroclip, Rotronic), with a stated relative humidity (RH) accuracy of $\pm$0.01$\times$RH and temperature accuracy of $\pm$0.1 K, located $\approx$1 cm from the mounted sample. The supersaturation, S = p_v/p_w, where p_v is the vapor saturation pressure and p_w is the saturation pressure corresponding to T_w, was controlled by adjusting the water reservoir temperature through which the N_2 was sparged. The uncertainty in the calculated S was determined from a propagation of error analysis. Droplet nucleation and growth was recorded at intervals of 0.1 seconds using a high-speed (CMOS) camera (Phantom v7.1, Vision Research), operating at a resolution of 800 x 600 and having a physical pixel size of 22 μm, attached to an upright microscope (Eclipse LV100, Nikon). Imaging was performed with either a 40$\times$ (NA = 0.6) (CFI S Plan Fluor ELWD, Nikon) or a 100$\times$ (NA = 0.7) (CFI L Plan EPI SLWD, Nikon) objective such that the field-of-view was 440 μm x 330 μm or 176 μm x 132 μm, respectively. The relationship between length and pixel count was calibrated with the known pillar spacing of a microstructured surface previously found using scanning electron microscopy.

ENVIRONMENTAL SCANNING ELECTRON MICROSCOPY CONDENSATION EXPERIMENTS

The details of the nucleation and growth of condensed droplets on the functionalized CuO surface were studied using an environmental scanning electron microscope (EVO 55 ESEM, Zeiss). Back scatter detection mode was used with a high gain. The saturated water vapor pressure in the ESEM chamber ranged from p_v = 800 - 1200 ± 75 Pa. Typical image capture was obtained with a beam potential of 20 kV and variable probe current depending on stage inclination angle. A 500 μm lower aperture was used in series with a 1000 μm variable pressure upper aperture for greater detail. The sample temperature was initially set to T_w = 277 - 281 ± 1.5 K using a cold stage and was allowed to equilibrate for 5 minutes. After equilibration, the surface temperature was decreased to 276 - 280 ± 1.5 K resulting in nucleation of water droplets on the sample surface due to condensation of the saturated water vapor. The typical supersaturation during imaging was S = 1.07 ± 0.1.

Images and recordings were obtained at an inclination angle of 70° to 80° from the horizontal and at a working distance ranging from 3 to 5 mm. The maximum resolution was ≈ 1 μm at an operating pressure of 800 Pa and increased with higher pressures. This specific setup was used to ensure good imaging of the droplet contact angle evolution on the condensing surface, not typically seen with overhead imaging, and to minimize substrate heating due to the electron beam [10]. Recordings were performed at 500 ms intervals, corresponding to a frame speed of two frames per second. To ensure good thermal contact between the sample and cold stage, copper tape was used for mounting.

RESULTS & DISCUSSION

Wetting dynamics

First, we studied the geometric evolution of individual droplets during condensation. In Figure 3a, the apparent contact angle behavior of condensed droplets growing on the hydrophobic CuO surfaces at $S = 1.07 \pm 0.1$ during ESEM imaging is shown. The ESEM images of water droplets showed strong topographic contrast allowing reliable contact angle measurements to be made [26]. Droplet contact angles were determined by fitting a circle to each individual droplet (spherical approximation) and determining the droplet radius R and the height of the spherical segment H. The contact angle was calculated from R and H as

$$\theta_{app} = \sin^{-1}\left(\frac{H - R}{R}\right) + 90°. \tag{4}$$

This image processing was more difficult for lower viewing angles due to the challenge in determining where the base of the droplet intersects the fitted circle, resulting in a larger error and fewer data points. The error associated with the droplet radius measurement was due to the limit of the image resolution (typically 200 – 500 nm). The CuO droplet morphology showed an initially varying contact angle ($R \leq 3$ - 4 μm) because of locally pinned contact lines at the droplet base. Radius-dependant contact angle behavior continued up to the point where the interface of the droplet made contact with surrounding nanostructures and began spreading over the surface in the Cassie state with an approximately constant advancing angle. The observed advancing angle compares reasonably well with the macroscopically measured value of $\theta_a^{CB} \approx 165°$. The early stage variation in the apparent contact angle was modeled as

$$\theta_{app}(R) = \cos^{-1}\left(\frac{r_p}{R}\right) + 90°,\tag{5}$$

assuming a fixed pinned base area of $A_p \approx \pi r_p^2$ underneath the individual droplets before coalescence as shown in the schematic in Figure 3b. Fitting Eq. (5) to the extracted contact angle data, we estimated that the characteristic radius of the pinned region to be $r_p \approx 1 - 2$ μm, which compares well with the characteristic spacing of the CuO nanostructures estimated as $l \approx \sqrt{\pi}d/(2\sqrt{\varphi_{eff}}) = 1.2$ μm with $d = 300$ nm and $\varphi_{eff} = 0.05$. This pinning behavior is consistent with previous studies of individual droplet growth on well-controlled nanopillar geometries [4, 14] and Cu(OH)$_2$ nanowires [9]. The droplet growth behavior on the hydrophobic CuO surfaces (Figure 3) was characteristic of the Cassie wetting state emerging from a pinned wetted region on the surface consistent with an estimated $E^*(r_{eff}) \approx 0.19$.

Next, we explored the influence of the nucleation density on the emergent wetting state captured using optical microscopy. Here, optical microscopy offers an advantage over ESEM since larger vapor pressures can be achieved without compromising image quality. In Figure 4a,b, condensation on the Au/thiolated surface at $S = 1.51 \pm 0.05$ resulted in a nucleation density of $N = 4 \times 10^9$ m^{-2}. The droplets were found to be weakly pinned to the surface as evidenced by the observation of droplet jumping (coalescing droplets disappeared from the field of view). Focusing through the droplets (Figure 4b) revealed that, in most cases, a single dark light absorbing region surrounded by a bright reflective ring was located beneath each droplet indicative of a partially-wetting Cassie state. The approximate sizes of the pinned base of the droplets were found by fitting circles to the dark regions. The magnification factor due to focusing through the nominally spherical droplets was estimated from $M = n/(2 - n) \approx 2$ [27], where a refractive index of $n = 1.33$ was used for water. Image processing of the measurements gave $r_p = 1.09 \pm 0.13$ μm consistent with the contact angle behavior

observed in Figure 3. In contrast, condensation on the silanated surface at $S \approx 1.48 \pm 0.05$ (Figure 4c,d) resulted in a nucleation density of $N > 5\text{x}10^{10}$ m^{-2} despite the fact that both the thiol and silane molecules are CF$_3$ terminated (i.e., same nominal surface energy). This large nucleation density led to the formation of highly pinned droplets that developed irregular shapes following coalescence events (*i.e.*, no coalescence-induced jumping observed). This behavior was in contrast to that observed at lower supersaturations in the ESEM where droplet jumping was observed on the silanated CuO surface (see Figure 4e). Focusing through the droplets (Figure 4d) showed a number of light absorbing and reflecting regions under the larger droplets formed by coalescence events consistent with a mixed mode wetting state [28] rather than complete wetting.

To understand this behavior, we first investigated the distribution of nucleation sites on the Au/thiol-functionalized surface. Figure 5a shows the location of nucleation sites (dots) on the Au/thiolated CuO surface captured using optical microscopy (Figure 4a,b). We analyzed the nucleation site distribution by measuring the nearest neighbor to each nucleation site as indicated by the arrows. ImageJ [29] was used to identify the coordinates of each nucleation site location. An algorithm was then implemented in Matlab (Mathworks) to identify each nucleation sites' nearest neighbor. Figure 5b shows that the distribution of nucleation sites was in good agreement with the Poisson distribution indicating a spatially random nucleation process where the mean nearest neighbor distance is given by [30]

$$\langle L \rangle = 0.5 N^{-0.5}$$

(6)

and the square root of the distribution variance is given by $\sqrt{\langle L \rangle}$. At this point, we note that the observation of nucleation at low supersaturations, $S \lesssim 1.5$, is inconsistent with kinetic nucleation theory, which predicts a critical supersaturation S_c > 2.5 for water condensing on hydrophobic surfaces ($\theta > 90°$) [20]. This discrepancy has been linked to randomly-distributed defects in the molecular film coatings used to impart hydrophobicity, which expose the underlying high-surface-energy substrate, in this case CuO, to create active nucleation sites [14, 31]. Thus, we attribute the distinctly different condensation behavior observed in Figure 4 to the defect density associated with the two functionalization methods and the resulting discrepancy in the number of active nucleation sites at $S \approx 1.5$.

The transition to a non-jumping mixed-mode wetting state regime can be understood by considering that, as the spacing between nucleation sites L approaches the length scale of the partially-pinned region under a droplet r_p, the excess surface energy released during coalescence due to a change in liquid/vapor interfacial area ΔA at constant volume V is

unable to overcome the constant work of adhesion associated with the pinned region under the coalescing droplets. Assuming that complete de-wetting of the liquid from the structured region is energetically unfavorable compared to some portion of the liquid remaining pinned within the structures on the surface, the work of adhesion required to create new interfacial area is $W_1/\gamma A_p = [(2-\varphi) + \varphi\cos\theta_r] \approx 2$ (for $\varphi \to 0$), where γ is the liquid/vapor interfacial tension,. To calculate the excess surface energy $\Delta E(\theta_{app}, R)$ available for droplet jumping we considered the situation shown in Figure 6a. Two droplets of equal diameter coalesce resulting in the formation of a single jumping droplet. Considering only the volume of liquid not pinned within the structure, the excess surface energy balance between states E_1 and E_2 is given by

$$\Delta E = \gamma(A_2 - A_1)$$
$$= \gamma\pi\left[4R^2(\cos\theta_{app}(R) - 1) - 4^{1/3}2^{2/3}\left(R^3(2 + \cos\theta_{app}(R))(\cos\theta_{app}(R) - 1)^2\right)^{2/3}\right],$$

(7)

where A is the liquid/vapor interfacial area and $\cos\theta_{app}(R)$ is obtained from Eq. (5). The total work of adhesion W was estimated based on the partially-wetted area under each droplet A_p. Neglecting the functionalized CuO contribution to W_1 since $\varphi \approx 0$, the work of adhesion for two droplets is then

$$W = 2W_1 = 4\gamma A_p.$$

(8)

When the magnitudes of ΔE and W are comparable or when W dominates ($|\Delta E/W| \lesssim 1$), there is little or no energy available in the system of the two droplets to power jumping. Thus, upon coalescence the newly formed droplet remains on the surface with either one or two wetted regions in the apparent base area, while the remainder of the apparent base area resides in the Cassie state (mixed mode wetting state). However, when $|\Delta E/W| \gg 1$, sufficient excess surface energy is available for conversion into the kinetic energy for droplet jumping, provided that other dissipation mechanism do not play a significant role [5].

In Figure 6b, $|\Delta E/W|$ is plotted as a function of the droplet coalescence length, $L = 2R$, scaled by the characteristic diameter of the pinned region beneath the droplet, $2r_p$, according to Eqs. (7) and (8). We observe that $|\Delta E/W| \sim \left[L/(2r_p)\right]^2$. For $r_p = 1$ μm, the model predicts $|\Delta E/W| = 0.07$ (no jumping) and $|\Delta E/W| = 6.27$ (jumping possible) for the silanated CuO ($\langle L\rangle/(2r_p) = 1.1$) and thiolated CuO ($\langle L\rangle/(2r_p) = 4.05$), respectively, consistent with the observed behavior in Figure 4. The horizontal bars for each point show $\pm\sqrt{\langle L\rangle}$. The large spread in separation distances indicates

the possibility of a mixed behavior of droplet jumping and pinning on the same surface. Increasing r_p from 1 μm to 2 μm reduces $|\Delta E/W|$ to ≈ 1.1 for the Au/thiol surface. For the silane surface, the same increase in r_p results in $\langle L \rangle/(2r_p) < 1$. Based on the observed jumping behavior of the Au/thiol surface and the mixed modes observed on the silane surface, we conclude that the pinned radius is in the range of $1\ \mu m \leq r_p \leq 1.5\ \mu m$, which is consistent with our optical measurements of the pinned base region.

Heat transfer modeling

To quantify the heat transfer behavior of individual droplets growing on the nanostructured CuO surface, we used a steady-state heat transfer model that captures the key thermal resistances from the saturated vapor atmosphere in the ESEM to the condensing structured surface for heat transferring through a single droplet [4, 32]. The geometry and thermal resistance network defined in the model in shown in Figure 7. The first resistances encountered as heat is transferred from the saturated vapor to the substrate are those associated with the droplet curvature (ψ_c) and liquid-vapor interface (ψ_i), which govern the kinetics of the phase change process. The depression of the saturation temperature due to the interface curvature leads to a thermal resistance given by [33],

$$\psi_c = \frac{1}{q}\frac{R_c}{R}(T_{sat} - T_S) = \frac{2T_{sat}\gamma}{Rh_{fg}\rho_w q}, \tag{9}$$

where q is the total heat transfer rate through the droplet, R_c is the critical nuclei radius, T_S is the depressed saturation temperature of the vapor near the liquid/vapor interface, h_{fg} is the latent heat and ρ_w is the liquid density. The thermal resistance between the curvature-depressed saturated vapor and the liquid at the liquid-vapor interface is given by

$$\psi_i = \left[h_i 2\pi R^2 (1 - \cos\theta_{app})\right]^{-1}. \tag{10}$$

The condensation interfacial heat transfer coefficient h_i is given by [17, 22]

$$h_i = \frac{2\alpha}{2-\alpha}(2\pi\mathcal{R}T_S)^{-1/2}\left(\frac{h_{lv}^2}{v_{lv}T_{sat}'}\right)\left(1 - \frac{p_v v_{lv}}{2h_{lv}}\right), \tag{11}$$

where $\mathcal{R} = 461.5$ J/kg.K and v_{lv} are the specific gas constant and the change in specific volume between the vapor and liquid phases of water, respectively. The locally reduced saturation temperature is given by $T_S = T_{sat} - \psi_c q$. The condensation coefficient, α, is the ratio of vapor molecules that will be captured by the liquid phase to the total number of vapor molecules reaching the liquid surface (ranging from 0 to 1). We assumed α = 0.9, which is appropriate for clean environments such as the ESEM [33], but in fact the model results were not sensitive to the condensation coefficient

ranging from 0.5 to 1 in this study. Equation (11) is strictly valid for $(q_i^{''} v_v / h_{lv})(2\mathcal{R}T_S)^{-1/2} \ll 1$, where $q_i^{''}/h_{lv}$ is the mass flux crossing the liquid/vapor interface. For the range of calculations performed here we found that the maximum $(q_i^{''} v_v / h_{lv})(2\mathcal{R}T_S)^{-1/2} \approx 1 \times 10^{-12}$. The latent heat released during phase change is then conducted through the droplet having a thermal resistance (ψ_d) that varies with θ_{app} (R) (Figure 3) given by [34]

$$\psi_d = \frac{\theta_{app}}{4\pi R k_w \sin\theta_{app}}.$$ (12)

Heat is then conducted from the apparent base of the droplet through the nanostructured region to the substrate through thermal resistances due to the hydrophobic coating (ψ_{hc}), the nanostructures (ψ_{CuO}), the area of pinned liquid underneath the droplet (ψ_w), and the underlying oxide (ψ_{Cu2O}). By approximating this composite region as a parallel heat transfer pathway from the apparent base of the droplet to the substrate surface we obtain

$$\left[\frac{1}{(\psi_{hc} + \psi_{CuO})} + \frac{1}{(\psi_w + \psi_{hc})} \right]^{-1} = \left[\pi R^2 k_{hc} \sin^2\theta_{app} \left(\frac{k_{CuO}\,\varphi}{\delta_{hc} k_{CuO} + \delta_{CuO} k_{hc}} + \frac{k_w(1-\varphi)}{\delta_{hc} k_w + \delta_{CuO} k_{hc}} \right) \right]^{-1}$$ (13)

where k_w is the thermal conductivity of water, k_{hc} is the thermal conductivity of the functional coating (≈ 0.2 W/m.K for a molecular monolayer) and δ_{hc} is the functional coating thickness (≈ 1 nm). Finally, the thermal resistance of the Cu_2O layer is given by

$$\psi_{Cu2O} = \frac{\delta_{Cu2O}}{\pi R^2 \sin^2\theta_{app}\, k_{Cu2O}}.$$ (14)

After summing Eqs. (9), (10), (12), (14) and rearranging, the heat transfer rate is

$$q = \frac{\pi R \left(\Delta T - \frac{2T_{sat}\gamma}{Rh_{lv}\rho_l} \right)}{h_{lv}\rho_l \left(\left[2h_i(1-\cos\theta_{app}) \right]^{-1} + \frac{\theta_{app} R}{4k_l \sin\theta_{app}} + \left[k_{hc} \sin^2\theta_{app} \left(\frac{k_{CuO}\,\varphi}{\delta_{hc} k_{CuO} + \delta_{CuO} k_{hc}} + \frac{k_l(1-\varphi)}{\delta_{hc} k_l + \delta_{CuO} k_{hc}} \right) \right]^{-1} + \frac{\delta_{Cu2O}}{\sin^2\theta_{app}\, k_{Cu2O}} \right)},$$ (15)

where ΔT is the temperature difference between the saturated vapor and the substrate temperature underneath the Cu_2O layer. The droplet heat transfer rate is then related to the droplet growth rate dR/dt by

$$q(R) = \dot{m} h_{lv} = \rho_l h_{lv} \frac{dV}{dt} = \pi \rho_l h_{lv} \frac{d}{dt} \left[\left(1 - \cos\theta_{app}(R) \right)^2 \left(2 + \cos\theta_{app}(R) \right) R^3 \right].$$ (16)

In this formulation, the apparent contact angle can be defined as a function of the drop radius as given by Eq. (5) [35]. Equating Eqs. (15) and (16), an expression for the droplet growth rate is obtained that is solved numerically to determine the droplet radius as a function of time [4]. To obtain sufficient accuracy and resolution, the time step used in the

numerical simulation was $\Delta t = 0.01$ s. Material properties were obtained using NIST software (REFPROP) [36] such that all input parameters used were temperature dependent.

In Figure 8a, the measured droplet radii as a function of time for 12 individual droplets were compared to the predictions of the heat transfer model described above. The data was best fit by $\Delta T = 0.034$ K, which is within the uncertainty of the measurements of temperature and pressure in the ESEM chamber. The results of the observed behavior compare well to the classic power law growth model for condensation [37]. When droplet dimensions are larger than the pinned region ($R \gtrsim 2$ μm), we expect the droplet radius to follow a power law over time $R = at^b$, where a is a constant, t is time and b, the power law exponent, ranges from 0 to 1 depending on the substrate dimensionality and growth limiting mechanism. During initial growth without coalescence ($R < 4$ μm), the power law exponent of $b = 3/4$ could be reasonably fitted to the data. This value was within the range of 0 to 1, but differs from $b = 1/3$ expected for diffusion limited growth. This result indicates that a diffusion process was not the major limiting growth mechanism. However, at long times the $b = 1/3$ growth exponent was recovered, coinciding with diffusion limited growth due to conduction through the droplet bulk.

Figure 8b gives a breakdown of the component thermal resistances normalized to the total thermal resistance predicted by the model during droplet growth. The model predicts that at small droplet radii ($R \lesssim 3$ μm), growth rates were limited by the combination of the conduction resistance of the droplet volume pinned within the nanostructures $(((\psi_{hc} + \psi_{CuO})^{-1} + (\psi_w + \psi_{hc})^{-1})^{-1})$ and the interface curvature resistance (ψ_c) that effectively reduces the driving pressure difference for vapor molecules attaching to the liquid-vapor interface. The interfacial resistance (ψ_i) was found to contribute little to the total resistance, peaking at $\psi_i/\psi_T = 0.17$ for $R = 0.95$ um before dropping off to $\psi_i/\psi_T < 0.01$ at larger radii. Similarly, the Cu_2O layer (ψ_{Cu2O}) beneath the CuO nanostructures also contributed negligibly to the total thermal resistance, $\psi_{Cu2O}/\psi_T \approx 0.02$. Beyond $R > 8$ μm, the heat transfer process was increasingly limited by the conduction resistance within the droplet bulk [4].

To estimate the overall heat transfer performance of the nanostructured CuO surface, the individual droplet growth behavior was incorporated into an expression for the droplet size distribution and integrating over all radii given by [4, 32]

$$q'' = \int_{R_c}^{\langle L \rangle/2} q(R)n(R)dR + \int_{\langle L \rangle/2}^{R_{max}} q(R)N(R)dR.$$

(17)

where $q"$ is the overall steady-state condensation heat transfer rate per unit area of the condensing surface, $\langle L \rangle /2$ is the mean droplet coalescence radius, $q(R)$ is the individual droplet heat transfer (Eq. (16)), $n(R)$ is the non-interacting droplet size distribution [34], $N(R)$ is the coalescence dominated droplet size distribution [38] and $R_{\max}$ is the droplet departure size. The first integral in Eq. (17) primarily captures the heat flux due to individual droplet growth before coalescence, but also accounts for the role of droplet sweeping $via\ n(R)$. The second integral captures the additional heat flux due to droplet coalescence and sweeping.

Equation (17) was used to make a predictive comparison of the heat flux performance of the silane-coated CuO surface to a corresponding smooth surface with a constant advancing contact angle of $\theta_a = 120°$. For the nanostructured CuO surface, we specified $\theta_a = 120°$ for $R_c \leq R \leq r_p$. Once $R = r_p$, Eq. (5) was then used to define θ_{app} up to the point where $\theta_{app} = \theta_a^{CB}$. With further increase in R at $\theta_{app} = \theta_a^{CB}$, the base area of the droplet in the Cassie state was treated as adiabatic. The mean droplet coalescence length $\langle L \rangle$ was varied by changing nucleation density according to Eq. (6). To make a conservative comparison of performance, we assumed that the nucleation density for both surfaces was equal which may not be the case due to the larger available surface area (large roughness) of the nanostructured CuO surface. For the flat surface, we assumed a fixed departure size comparable to the capillary length, $R_{max} = 2$ mm. The departure radius for droplets on the silanized CuO surface was equated to $\langle L \rangle /2$ assuming ideal coalescence-induced jumping behavior, $i.e.$, in the inviscid limit with no influence of variable contact angle or surface adhesion. The assumption that droplet jumping is the only shedding mechanism on the nanostructured CuO surface leads to neglecting the second term in Eq. (17) and a simplification of $n(R)$ since the sweeping period, $\tau \rightarrow \infty$.

To place into context the theoretical model, we extracted the mean coalescence length $\langle L \rangle$ from the ESEM imaging experiments. To estimate the time-averaged $\langle L \rangle$ for condensed droplets on the silanated CuO surface, the droplet size distribution was obtained from the ESEM images. Droplet number density and diameters were measured from multiple images of the steady-state condensation process, accounting for inclination angle (Figure 9). As a result of the high number density of droplets, $n \approx 1.28 \times 10^{10}$ m^{-2}, the mean center-to-center spacing of the droplets was estimated as $\langle L \rangle \approx$ 4.42 μm from Eq. (6). Due to coalescence-induced jumping maintaining the vast majority of the droplet distribution below 10 μm (≈ 90 %), this spacing was maintained approximately constant resulting in a constant mean droplet size $(b_{global} \approx 0)$ [5, 14].

In Figure 10a, the heat flux ratio is plotted as a function of a unique coalescence length scaled by the pinned base diameter of the droplet for the cases where r_p = 1 μm, 1.5 μm and 2 μm. Thus, the minimum allowable L corresponds to $L/2r_p$ = 1 for the three cases. Figure 10 demonstrates that for r_p = 1 μm, the CuO surface degrades heat transfer performance in comparison to the smooth surface over the entire range of allowable coalescence lengths. For r_p = 1.5 − 2 μm, q_{CuO}''/q_F'' = 1.13 − 1.25 at $L/(2r_p)$ = 1, but drops off steadily as L increases. This behavior is compared to a hypothetical surface with the CuO structure height reduced to δ_{CuO} = 100 nm. Here we see that the heat transfer behavior is enhanced at $L/(2r_p)$ = 1 for the three values of r_p modeled, ranging from $1.16 \le q_{CuO}''/q_F'' \le 1.87$. This result highlights the important role of the parasitic thermal resistance associated with the height of the structures. The inset of Figure 10a shows the predicted behavior for the three pinned regions sizes for the average spacing identified in Figure 9, $\langle L \rangle$ = 4.42 μm. The model predicts q_{CuO}''/q_F'' = 0.37, 0.7 and 1.11 for r_p = 1 μm, 1.5 μm and 2μm, respectively.

The predicted behavior in Figure 10a is a direct result of the dominant thermal resistances as a function of droplet size. During early stages of growth ($R \lesssim 6$ μm), the conduction resistance (ψ_d) through the droplet is relatively small compared to the conduction resistance through the pinned base region and the curvature resistance. This explains the significant effect of reducing the nanostructure height while assuming identical contact angle behavior. Therefore, droplet shedding at these radii isolates a regime of high growth rates (in comparison to the later diffusion limited growth), but can only be accessed in the jumping-droplet regime by reducing the characteristic length-scale of the surface structures. In the diffusion limited growth regime ($R \gtrsim 6$ μm), the performance of the nanostructured CuO surface is penalized by the large apparent contact angle of the droplets, which causes significant thermal resistance due to the limited droplet basal contact area in comparison to a droplet on the smooth condensing surface.

In Figure 10b and c, the heat flux ratio is plotted as a function of $L/(2r_p)$ for r_p = 1.5 μm and (b) δ_{CuO} = 1.5 μm and (c) δ_{CuO} = 100 nm with 0.01 K ≤ ΔT ≤ 0.05 K in steps of 0.01 K. Figure 10d summarizes the results shown in Figure 10b and c. We can see that the jumping surface is more strongly affected by the degree of subcooling in comparison to the smooth surface. The strong effect of subcooling can be explained by the fact that jumping droplets grow in size ranges from R_c up to $\langle L \rangle/2$ (≈ 1 - 10 μm) where the curvature resistance is appreciable during the majority of the droplet growth. However, shedding droplets obtain most of their growth and heat transfer at size ranges from R_c up to ≈ 1mm) where the curvature resistance is a smaller contribution to the thermal resistance. The result is a heavier penalty paid by jumping

droplets, especially at low supersaturations. We observe this behavior in the model by recalling that the heat transfer behavior of a jumping surface is dictated solely by the first integral in Eq. (17), whereas in conventional dropwise condensation the heat transfer behavior is more heavily weighted by the second integral in Eq. (17) and the important role of sweeping during droplet shedding. Thus, the $\Delta T - (2T_{sat}\gamma/Rh_{lv}\rho_l)$ term in Eq. (15) plays a more central role in the heat transfer behavior of jumping droplet condensation surfaces.

CONCLUSIONS

A scalable synthesis method for creating unique oxide nanostructures capable of providing sustained superhydrophobic condensation once properly functionalized was presented. Spatially random nucleation at low supersaturations ($S \leq 1.5$) was confirmed using optical microscopy, suggesting the role of randomly distributed defects in the molecular coatings on the nucleation process. A wetting model was derived showing the increasing role of surface adhesion as separation distances between droplets are reduced to scales comparable to the pinned diameter at the base of the condensed droplets. This leads to the suppression of droplet jumping even before reaching the Wenzel transition. Observations of nucleation and growth behavior captured using ESEM, coupled with a model of the heat transfer process on superhydrophobic CuO surfaces, suggest that these surfaces may only become advantageous over a smooth hydrophobic surface for nucleation densities corresponding to $L/(2r_{\rm p}) \rightarrow 1$ with $r_p \gtrsim 1.5$ μm. This result is due predominantly to the increased resistance associated with the large apparent contact angles demonstrated by drops on the CuO surface, the height of the nanostructures and the assumption of comparable nucleation densities for both the structured and smooth condensing surfaces. This last assumption may be overly conservative given the large roughness of the CuO surface. Indeed, we have recently demonstrated, *via* macroscopic heat transfer measurements, that these surfaces are capable of providing a 1.25× heat flux enhancement compared to a conventional dropwise condensing surface [39]. Good agreement between the data and the model was obtained by taking the nucleation density on the CuO surface to be three times larger than the corresponding smooth surface. Furthermore, we note that, presently, the overall heat transfer model does not account for the range of droplet separation distances characteristic of a random distribution. This point remains to be addressed in future studies.

In addition to demonstrating the benefits of increased nucleation density and smaller structure length scales, these results suggest that the coalescence-induced jumping mechanism for droplet departure should be studied in more detail to

understand the trade-off between efficient shedding and $L/(2r_\mathrm{p})$ ratios as they approach unity, marking the transition to Wenzel behavior for the partial wetting state. While this work highlights some of the challenges associated with realizing superhydrophobic surfaces that can enhance condensational heat transfer, we emphasize that there remains significant opportunities to engineer condensation behavior by manipulating surface structures at nanometer length scales.

NOMENCLATURE

A Liquid/vapor interfacial area [m^2]

A_p Droplet base pinned area [m^2]

a Power law constant [m/s]

b Power law exponent [-]

E Surface energy [J]

ΔE Change in surface energy [J]

E^* Wetting-state energy ratio [-]

H Spherical segment height [m]

h_i Interfacial heat transfer coefficient [W/m^2.K]

h_lv Latent heat [J/kg]

k Thermal conductivity [W/m.K]

l Characteristic structure spacing/pitch [m]

$\langle L \rangle$ Mean coalescence (nearest neighbor) length [m]

L Coalescence (nearest neighbor) length [m]

M Magnification factor [-]

N Nucleation density [m^{-2}]

n Droplet number density [m^{-2}], refractive index [-]

$N(R)$ Coalescence-dominated droplet size distribution [m^{-2}]

$n(R)$ Non-interacting droplet size distribution [m^{-2}]

P Cumulative probability [-]

p_v Vapor saturation pressure [Pa]

Corresponding authors: ryan.enright@alcatel-lucent.com, enwang@mit.edu

p_w Saturation pressure corresponding to T_w [Pa]

Q Flow rate [L/min]

q Heat transfer rate [W]

q'' Heat flux [W/m^2]

r Surface roughness[-]

r_p Droplet pinned base radius [m]

R Droplet radius [m]

$\mathcal{R}$ Specific gas constant [J/kg.K]

S Supersaturation (p_v/p_w) [-]

t Time [s]

T_w Wall temperature [K]

T_S Curvature-depressed vapor temperature [K]

ΔT Temperature difference between the liquid-vapor interface and the droplet base [K]

W_I Single droplet work of adhesion [J]

W Two droplet work of adhesion [J]

Greek Symbols

α Condensation coefficient [-]

γ Surface tension [N/m]

δ Thickness/height [m]

θ Contact angle, x-ray diffraction angle [°]

$\Delta\theta$ Contact angle hysteresis [°]

ρ_l Liquid density [kg/m^3]

τ Sweeping period [s]

ν_v Vapor specific volume [m^3/kg]

ν_{lv} Change in specific volume between vapor and liquid phases [m^3/kg]

φ Solid fraction [-]

ψ Thermal resistance [W/K]

Superscripts

CB   Cassie-Baxter

W   Wenzel

Subscripts

a   Advancing

app   Apparent

c   Curvature, critical

d   Droplet

e   Equilibrium

eff   Effective

F   Flat

g   Pinned liquid region under droplet

hc   Hydrophobic coating

i   Liquid-vapor interface

max   Maximum

n   Nanostructure

r   Receding

sat   Saturation

T   Total

w   Water

Acronyms

ESEM Environmental scanning electron microscope

NA   Numerical aperture

RH   Relative humidity

ACKNOWLEDGMENTS

REFERENCES

[1] Beér, J. M., 2007, "High efficiency electric power generation: The environmental role," Progress in Energy and Combustion Science, 33(2), pp. 107-134.

[2] Khawaji, A. D., Kutubkhanah, I. K., and Wie, J. M., 2008, "Advances in seawater desalination technologies," Desalination, 221(1-3), pp. 47-69.

[3] Pérez-Lomabard, L., Ortiz, J., and Pout, C., 2008, "A review on buildings energy consumption information " Energy and Buildings, 40(3), pp. 394-398.

[4] Miljkovic, N., Enright, R., and Wang, E. N., 2012, "Effect of droplet morphology on growth dynamics and heat transfer during condensation on superhydrophobic nanostructured surfaces," ACS Nano, 6(2), pp. 1776-1785.

[5] Boreyko, J. B., and Chen, C.-H., 2009, "Self-propelled dropwise condensate on superhydrophobic surfaces," Phys. Rev. Lett., 103(18), pp. 184501.

[6] Dietz, C., Rykaczewski, K., Fedorov, A., and Joshi, Y., 2010, "ESEM Imaging of Condensation on a Nanostructured Superhydrophobic Surface," J. Heat Transfer, 132(8), pp. 080904.

[7] Dietz, C., Rykaczewski, K., Fedorov, A. G., and Joshi, Y., 2010, "Visualization of droplet departure on a superhydrophobic surface and implications to heat transfer enhancement during dropwise condensation," Appl. Phys. Lett., 97(3), pp. 033104 - 033104-3.

[8] Rykaczewski, K., Osborn, W. A., Chinn, J., Walker, M. L., Scott, J. H. J., Jones, W., Hao, C., Yao, S., and Wang, Z., 2012, "How nanorough is rough enough to make a surface superhydrophobic during water condensation?," Soft Matter, 8(pp. 8786-8794.

[9] Rykaczewski, K., and Scott, J. H. J., 2011, "Methodology for imaging nano-to-microscale water condensation dynamics on complex nanostructures," ACS Nano, 5(7), pp. 5962-5968.

[10] Rykaczewski, K., Scott, J. H. J., and Fedorov, A. G., 2011, "Electron beam heating effects during environmental scanning electron microscopy imaging of water condensation on superhydrophobic surfaces," Appl. Phys. Lttrs., 98(9), pp. 093106 - 093106-3.

[11] Rykaczewski, K., Scott, J. H. J., Rajauria, S., Chinn, J., Chinn, A. M., and Jones, W., 2011, "Three dimensional aspects of droplet coalescence during dropwise condensation on superhydrophobic surfaces," Soft Matter, 7(19), pp. 8749-8752.

[12] Feng, J., Pang, Y., Qin, Z., Ma, R., and Yao, S., 2012, "Why condensate drops can spontaneously move away on some superhydrophobic surfaces but can not on others?," ACS Appl. Mater. Interfaces, 10.1021/am301767k.

[13] Feng, J., Qin, Z., and Yao, S., 2012, "Factors affecting the spontaneous motion of condensate drops on superhydrophobic copper surfaces," Langmuir, 28(14), pp. 6067-6075.

[14] Enright, R., Miljkovic, N., Al-Obeidi, A., Thompson, C. V., and Wang, E. N., 2012, "Condensation on superhydrophobic surfaces: The role of local energy barriers and structure length scale," Langmuir, 28(40), pp. 14424-14432.

[15] Cassie, A. B. D., and Baxter, S., 1944, "Wettability of porous surfaces," Trans. Faraday Soc., 40, pp. 546 - 541

[16] Wenzel, R. N., 1936, "Resistance of solid surfaces to wetting by water," Ind. Eng. Chem., 28, pp. 988 - 994

[17] Choi, W., Tuteja, A., Mabry, J. M., Cohen, R. E., and Mckinley, G. H., 2009, "A modified Cassie-Baxter relationship to explain contact angle hysteresis and anisotropy on non-wetting textured surfaces," J. Colloid Interface Sci., 339(1), pp. 208-216.

[18] Brisard, G. M., Rudnicki, J. D., Mclarnon, F., and Cairns, E. J., 1995, "Application of probe beam deflection to study the electrooxidation of copper in alkaline media," Electrochimica Acta, 40(7), pp. 859-865.

[19] Drogowska, M., Brossard, L., and Ménard, H., "Influence of anions on the passivity behavior of copper in alkaline solutions," Surface and Coatings Technology, 34(4), pp. 383-400.

[20] Kashchiev, D., 2000, *Nucleation: Basic Theory with Applications*, Butterworth-Heinemann, Oxford.

[21] Cao, L., Jones, A. K., Sikka, V. K., Wu, J. Z., and Gao, D., 2009, "Anti-icing superhydrophobic coatings," Langmuir, 25(21), pp. 12444-12448.

[22] Gibbs, J. W., Bumstead, H. A., and Van Name, R. G., 1906, *The scientific papers of J. Willard Gibbs*, Longmans, Green and co., New York and Bombay.

[23] Quéré, D., 2008, "Wetting and Roughness," Annual Review of Materials Research, 38(1), pp. 71-99.

[24] Kwak, K., and Kim, C., 2005, "Viscosity and thermal conductivity of copper oxide nanofluid," Korea-Aust Rheol J, 17(2), pp. 35-40.

[25] Blow, M. L., Kusumaatmaja, H., and Yeomans, J. M., 2009, "Imbibition through an array of triangular posts," J. Phys.: Condens. Matter, 21(46), pp. 464125.

[26] Donald, A. M., Stelmashenko, N. A., Craven, J. P., Terentjev, E. M., and Thiel, B. L., 2001, "Topographic contrast of partially wetting water droplets in environmental scanning electron microscopy," Journal of Microscopy-Oxford, 204(2), pp. 172-183.

[27] Wang, Z., Guo, W., Li, L., Luk'yanchuk, B., Khan, A., Liu, Z., Chen, Z., and Hong, M., 2010, "Optical virtual imaging at 50 nm lateral resolution with a white-light nanoscope," Nature Communications, 2, 218.

[28] Wier, K. A., and Mccarthy, T. J., 2006, "Condensation on ultrahydrophobic surfaces and its effect on droplet mobility: ultrahydrophobic surfaces are not always water repellant," Langmuir, 22(6), pp. 2433-2436.

[29] Schneider, C. A., Rasband, W. S., and Eliceiri, K. W., 2012, "NIH Image to ImageJ: 25 years of image analysis," Nature Methods, 9, pp. 671-675

[30] Gaertner, R. D., 1963, "Distribution of active sites in the nucleate boiling of liquids," Chem. Eng. Prog., 59, pp. 52-61

[31] Cao, P., Xu, K., Varghese, J. O., and Heath, J. R., 2011, "The microscopic structure of adsorbed water on hydrophobic surfaces under ambient conditions," Nano Lett., 11(12), pp. 5581-5586.

[32] Miljkovic, N., Enright, R., and Wang, E. N., 2012, "Growth dynamics during dropwise condensation on nanostructured superhydrophobic surfaces," Proceedings of the 3rd Micro/Nanoscale Heat & Mass Transfer International Conference, Atlanta, GA, USA, March 3-6.

[33] Carey, V. P., 2008, *Liquid-Vapor Phase-Change Phenomena*, Taylor & Francis Group, LLC, New York & Oxen.

[34] Kim, S., and Kim, K. J., 2011, "Dropwise condensation modeling suitable for superhydrophobic surfaces " J. Heat Transfer, 133(8), pp. 081502-1 - 081502-7.

[35] Miljkovic, N., Enright, R., and Wang, E. N., 2013, "Modeling and optimization of condensation heat transfer on micro and nanostructured superhydrophobic surfaces," J. Heat Transfer, in press.

[36] Lemmon, E. W., Mclinden, M. O., and Friend, D. G., 2005, NIST Chemistry WebBook, NIST Standard Reference Database Number 69, National Institute of Standards and Technology, Thermophysical properties of fluid systems.

[37] Fritter, D., Knobler, C. M., and Beysens, D. A., 1991, "Experiments and simulations of the growth of droplets on a surface (breath figures)," Phys. Rev. A, 43(6), pp. 2858-2869.

[38] Rose, J. W., and Glicksman, L. R., 1973, "Dropwise condesation - The distribution of drop sizes," Int. J. Heat Mass Tran., 16(2), pp. 411-425.

[39] Miljkovic, N., Enright, R., Nam, Y., Lopez, K., Dou, N., Sack, J., and Wang, E. N., 2012, "Jumping-droplet-enhanced condesation on scalable superhydrophobic nanostructured surfaces," Nano Lett., 13(1), pp. 179-187.

Figure 1 SEM images (a-b) and XRD pattern (c) of the copper oxide nanostructures, after 1 min (a) and 5 min (b-c) of oxidation. (d) SEM image of a FIB milled sample showing a cross-section of the nanostructured copper surface after a 10 minute oxidation step. The arrows indicate the approximate extent of the Cu_2O and $Cu_2O + CuO$ regions.

Figure 2 Schematic of the optical microscopy experimental set-up. Dry N_2 was supplied from a cylinder with the flow rate measured using a rotometer. A three-way valve was used to route the N_2 supply either directly to the enclosure or through a temperature-controlled water reservoir *via* a sparging head and then to the enclosure. The enclosure humidity was monitored using a humidity probe located ~1 cm from the mounted sample. Images were captured at either 40× or 100× magnification using a CMOS camera mounted to an upright microscope.

Figure 3 Droplet apparent contact angle as a function of the droplet diameter extracted from the ESEM data on the Au/thiol (**O**) and silane (**□**) functionalized CuO surfaces ($p_v = 1300 \pm 75$ Pa, $T_w = 283 \pm 1.5$ K, $S = 1.07 \pm 0.1$). The solid curve is defined as $\theta_{app} = \cos^{-1}(r_p/R) + 90°$ with $r_p = 1.5$ μm. The dashed dot curves represent the bounds of Eq. (5) for $r_p = 1.5 \pm 0.5$ μm. The horizontal dashed line represents the macroscopically measured apparent contact angle, $\theta_{app} \approx 165°$. The inset shows a typical ESEM image captured during the droplet growth process on the silane functionalized CuO surface. (b) Diagram showing the evolution of the droplet shape predicted by Eq. (5) for $90° \leq \theta_{app} \leq 170°$ in steps of 20° (droplets bounded by solid curves). Once the advancing state is reached the droplet grows with constant θ_{app} (droplet bounded by dashed curve).

Figure 4 Emergent droplet morphology on the functionalized CuO surfaces in the coalescence-dominated growth stage. Partially-wetting Cassie behavior with jumping droplets emerged on the Au/thiolated CuO surface where $\langle L \rangle = 0.5N^{-0.5} \approx 8.1$ μm obtained by (a) focusing at the surface (top) and confirmed by (b) focusing through the droplets (below) to show the wetting state ($S = 1.51 \pm 0.05$, $N = 3.83 \times 10^9$ m^{-2}). The red arrow in the inset of (b) points to a light-absorbing region surrounded by a light-reflecting region indicative of the partial-wetting morphology (Inset scale bar: 10 μm). Mixed-mode wetting behavior with pinned droplets on the silanated CuO surface where $\langle L \rangle = 0.5N^{-0.5} < 2.2$ μm obtained by (c) focusing at the surface (top) and confirmed by (d) focusing through the droplets (below) to show the wetting state ($S = 1.48 \pm 0.05$, $N > 5 \times 10^{10}$ m^{-2}). (e) Time-lapse images of condensation on the silane-coated CuO surface during ESEM imaging. The dashed and solid circles indicate droplet groups before and after coalescence, respectively. ESEM conditions: $p_v = 800 \pm 75$ Pa and $T_w = 276 \pm 1.5$ K ($S = 1.07 \pm 0.1$).

Figure 5 Nucleation site spatial distribution. (a) Coordinate map showing the position of the nucleation sites (**●**) and arrows indicating their nearest neighbor captured using optical microscopy at 100x magnification on the Au/thiol functionalized CuO surface at $t = 10$ s after the start of the experiment ($S = 1.51 \pm 0.05$, $N = 3.83 \times 10^9$ m^{-2}). (b) Cumulative probability distribution of the nucleated droplet nearest neighbors (**O**) compared to the predictions for a random distribution, $P = 1 - e^{-N\pi L^2}$ (solid line). The mean separation distance between nucleation sites is given by $2L\sqrt{N} = 1$. The horizontal bars represent the bin width.

Figure 6 Droplet jumping to pinning transition. (a) The excess liquid/vapor surface energy was estimated by considering the difference in energy between states E_1 and E_2. Energy is required to overcome the work of adhesion to form a liquid/vapor interface of area $2A_p$ for the two pinned necks of the coalescing droplets. (b) Excess surface energy compared to the work of adhesion, $|\Delta E/W|$, as a function of the droplet separation distance, L, divided by the droplet pinned base diameter, $2r_p$. Three values of r_p (= 1 μm, 1.5 μm and 2 μm) are shown for each surface. Increasing r_p results in smaller values of $|\Delta E/W|$. For $r_p = 1$ μm, the model predicts $|\Delta E/W| = 0.07$ and $|\Delta E/W| = 6.27$ for the silanated CuO ($\langle L \rangle/(2r_p) = 1.1$, **□**) and thiolated CuO ($\langle L \rangle/(2r_p) = 4.05$, **O**), respectively. The shaded region ($\langle L \rangle/(2r_p) \leq 1$) marks the transition to the Wenzel state. The horizontal bars for each point show $\pm\sqrt{\langle L \rangle}$.

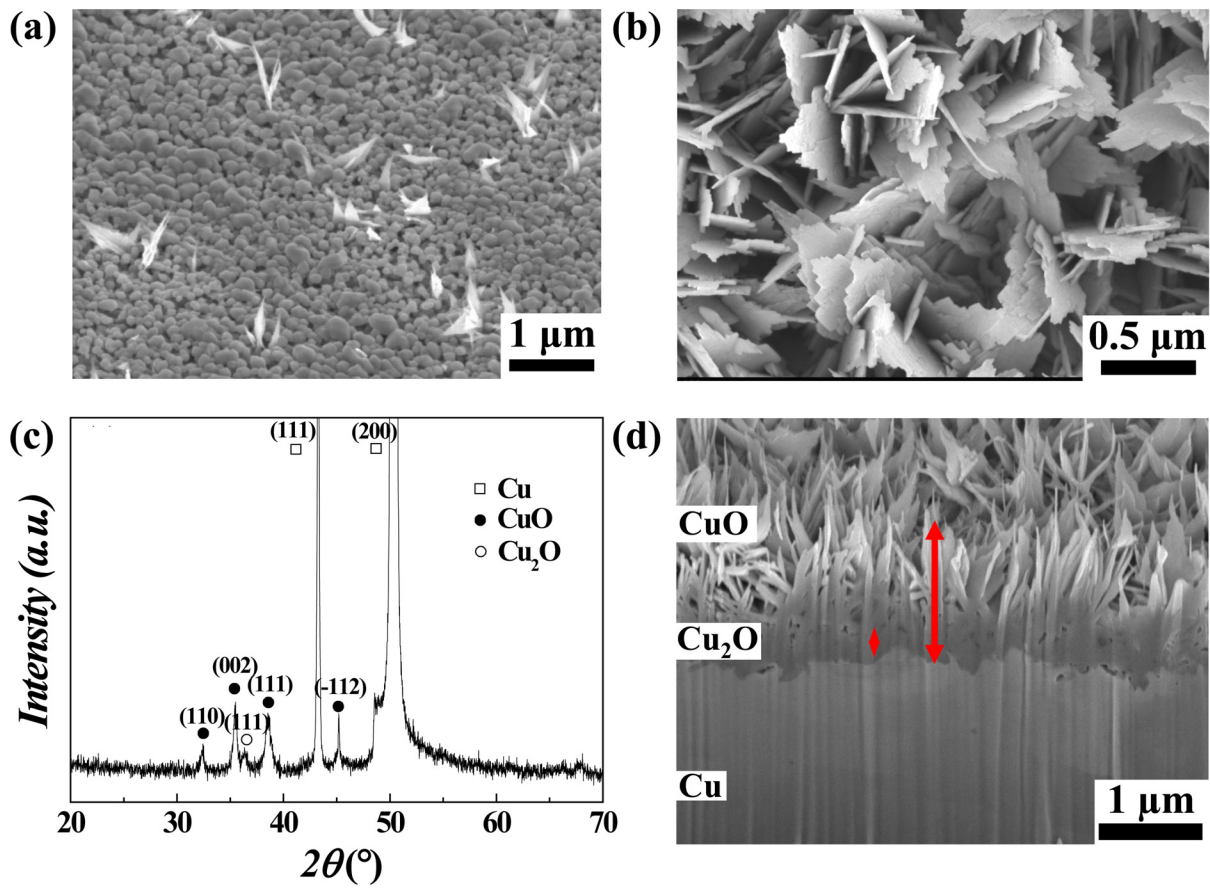Corresponding authors: ryan.enright@alcatel-lucent.com, enwang@mit.edu

Figure 7 Individual droplet heat transfer model. (a) Schematic of the droplet on the condensing surface growing in the partially-wetting morphology. (b) Droplet thermal resistance diagram showing the droplet curvature (ψ_c), liquid-vapor interface (ψ_i), droplet conduction (ψ_d), hydrophobic coating (ψ_{hc}), CuO nanostructure (ψ_{CuO}), liquid bridge (ψ_w) and Cu_2O under layer (ψ_{Cu2O}) thermal resistances.
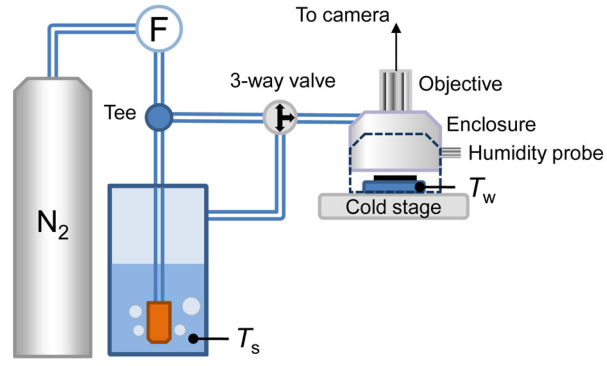
Figure 8 Model prediction of individual drop growth rates averaged for 12 individual droplets. (a) The experimentally measured droplet diameters as a function of time (O) are compared to the individual droplet growth model (solid curve) with $r_p = 1.5$ μm, $\delta_{CuO} = 1.5$ μm. ESEM conditions: $p_v = 800 \pm 75$ Pa and $T_w = 276 \pm 1.5$ K ($S = 1.07 \pm 0.1$). Model solutions were obtained for $\Delta T = 0.034$ K, which was within the uncertainty of the measured temperatures and pressures in the ESEM chamber. This value was chosen based on the best fit between the model and experimental growth rate data. The inset shows the experimental data, the model predictions and a fitted $R \propto t^{1/3}$ scaling (dashed curve) in log coordinates. The error bars correspond to uncertainty in the measured droplet radius. (b) The key thermal resistances normalized to the total thermal resistance corresponding to (a) as a function of droplet radius. The vertical line delineates the transition from radius-dependant apparent contact angle ($\theta_{app}(R)$) to a fixed contact angle equal to the macroscopically measured apparent advancing contact angle (θ_a^{CB}) at $2R = 11$ μm. The thermal resistance components indicated in the plot are the conduction resistance of the droplet volume pinned within the nanostructures, $(((\psi_{hc} + \psi_{CuO})^{-1} + (\psi_w + \psi_{hc})^{-1})^{-1})$, the interface curvature resistance (ψ_c), the interfacial resistance (ψ_i), the Cu_2O layer resistance (ψ_{Cu2O}) and the droplet bulk resistance (ψ_d).

Figure 9 Droplet number density as a function of droplet diameter for steady-state condensation averaged over several cycles of droplet growth, coalescence-induced jumping and re-growth for ESEM conditions: $p_v = 800 \pm 75$ Pa, $T_w = 276 \pm 1.5$ K, $S = 1.07 \pm 0.1$. Summing over the range of droplet diameters gives a total droplet number density $n = 1.28 \times 10^{10}$ m^{-2} corresponding to $\langle L \rangle = 4.42$ μm according to Eq. (6). The counting error associated with the droplet number density was estimated to be ~10% at each size range.

Figure 10 Overall heat transfer behavior. (a) Predicted overall heat flux ratio q''_{CuO}/q''_F as a function of scaled droplet coalescence length $L/(2r_p)$ for the CuO nanostructured surface ($\delta_{CuO} = 1.5$ μm) compared to a smooth hydrophobic surface for $r_p = 1$ μm, 1.5 μm and 2 μm (solid curves). The CuO surface shows an enhancement for $L/(2r_p) \to 1$ and $r_p \geq 1.5$ μm. This behavior is compared to a similar, hypothetical surface with the CuO height reduced to $\delta_{CuO} = 100$ nm (dashed curves). The hypothetical surface demonstrates a wider range of enhancement. Modeled conditions: $\Delta T = 0.034$ K, $p_v = 800$ Pa. The inset shows the predicted heat transfer behavior $r_p = 1$ μm, 1.5 μm and 2 μm with $\langle L \rangle = 4.42$ μm. Predicted overall heat flux ratio q''_{CuO}/q''_F as a function of droplet coalescence length L with (b) $\delta_{CuO} = 1.5$ μm and (c) $\delta_{CuO} = 100$ nm for a range of driving temperature differences (0.01 K $\leq \Delta T \leq 0.05$ K in steps of 0.01 K) with constant $p_v = 800$ Pa. (d) The values of q''_{CuO}/q''_F at $L/(2r_p) = 1$ (solid curves) and $|q''_{CuO}/q''_F|_{max}$ (dashed curves) for $\delta_{CuO} = 1.5$ μm (□) and $\delta_{CuO} = 100$ nm (O) obtained from (b) and (c), respectively.

Fig_1.tif

Fig_2.tif
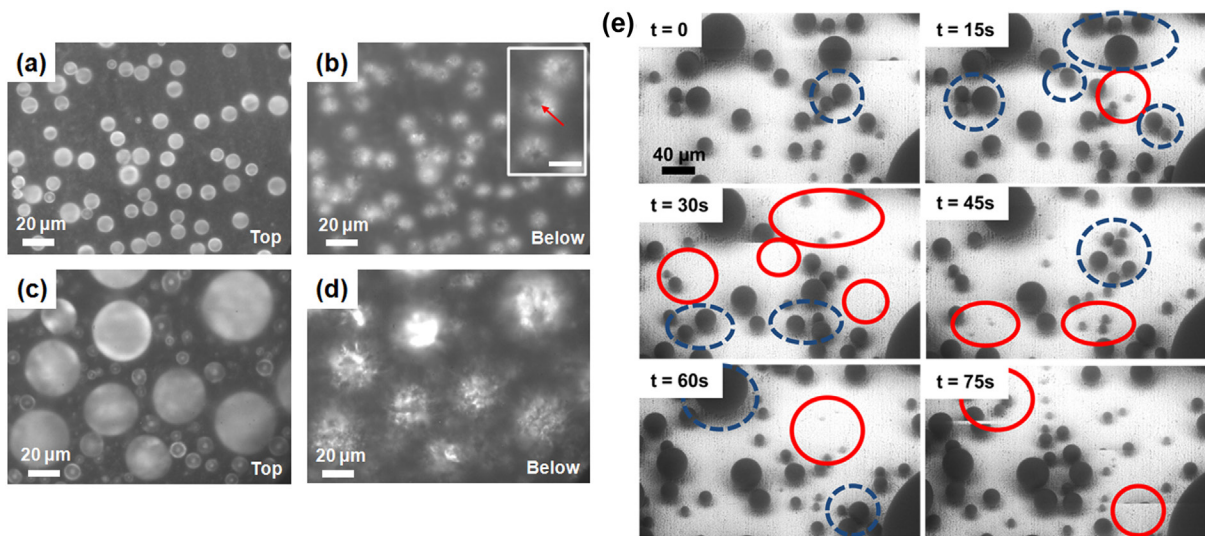
(a)

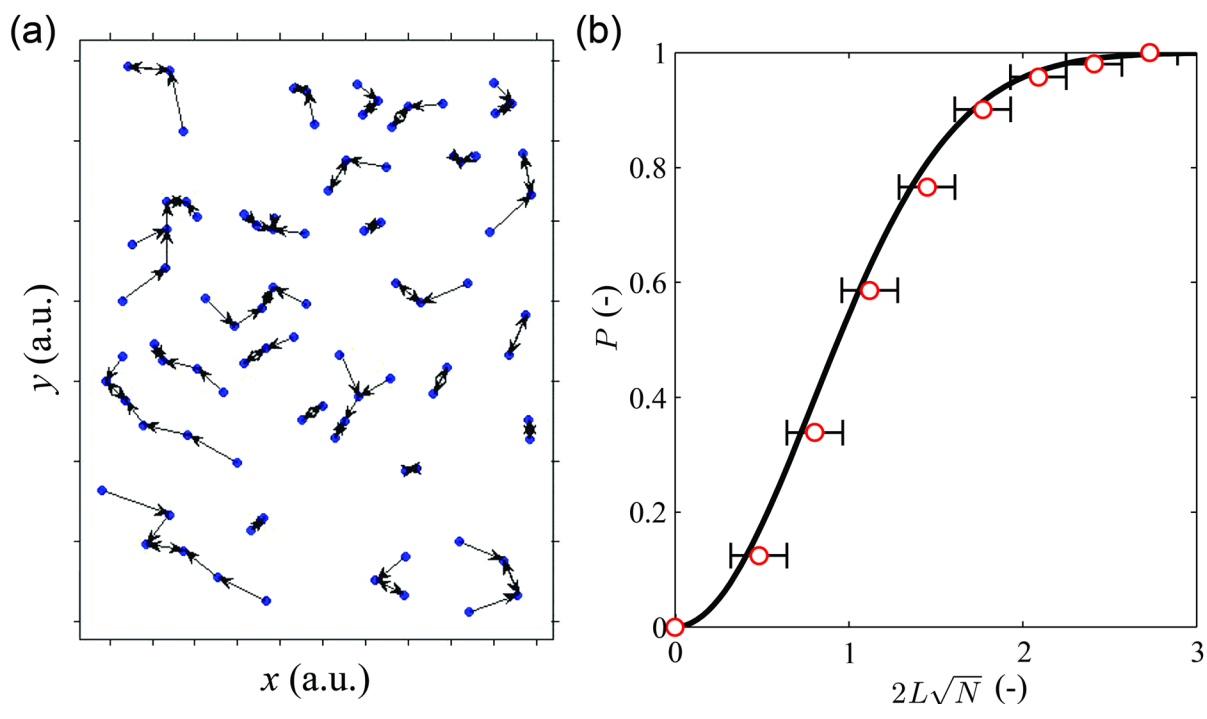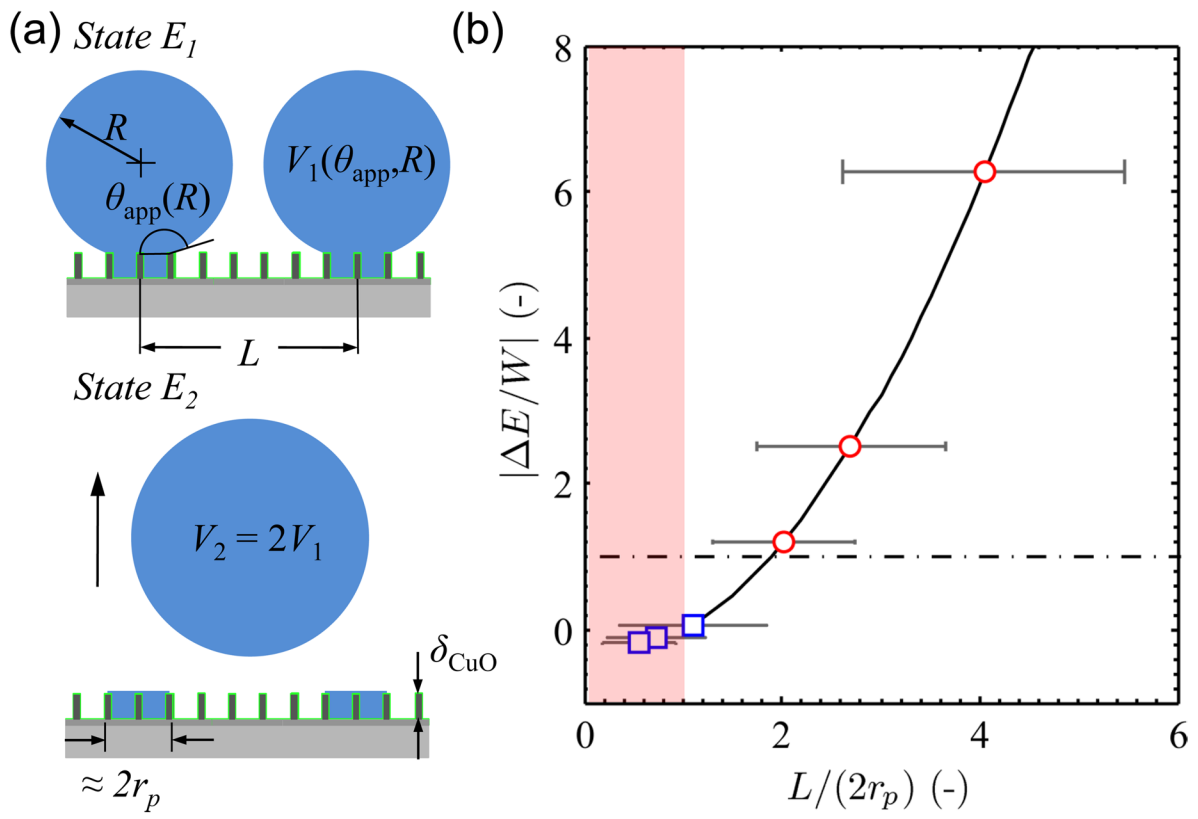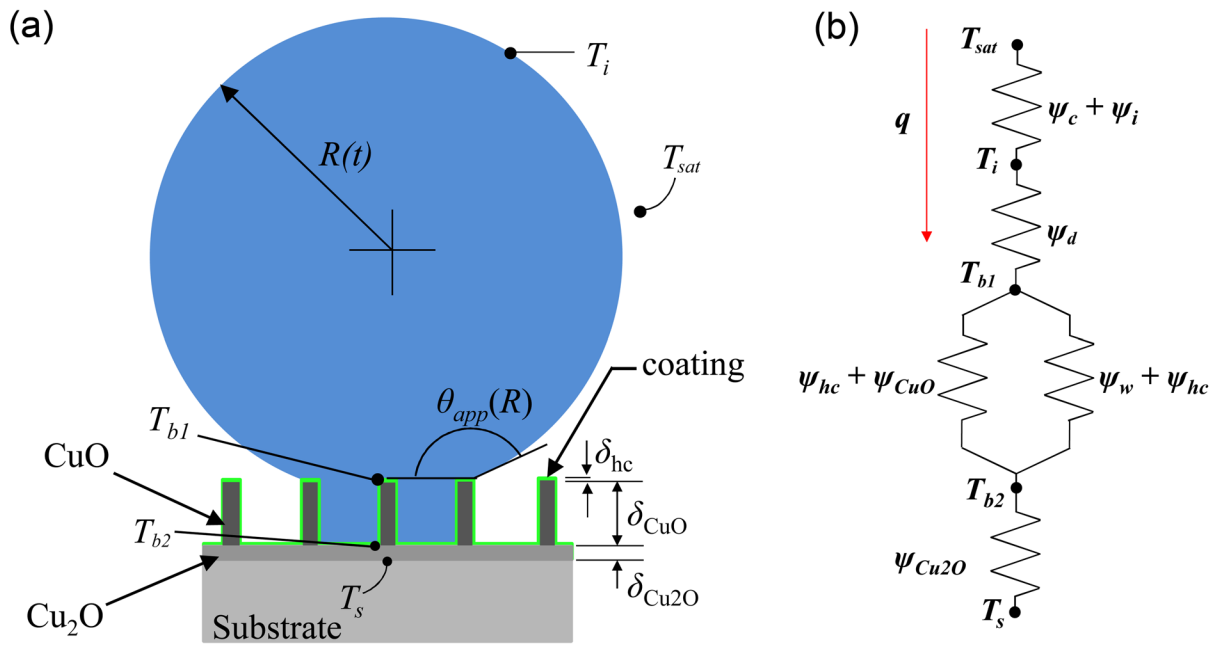(b)

Fig_3.tif

Fig_4.tif
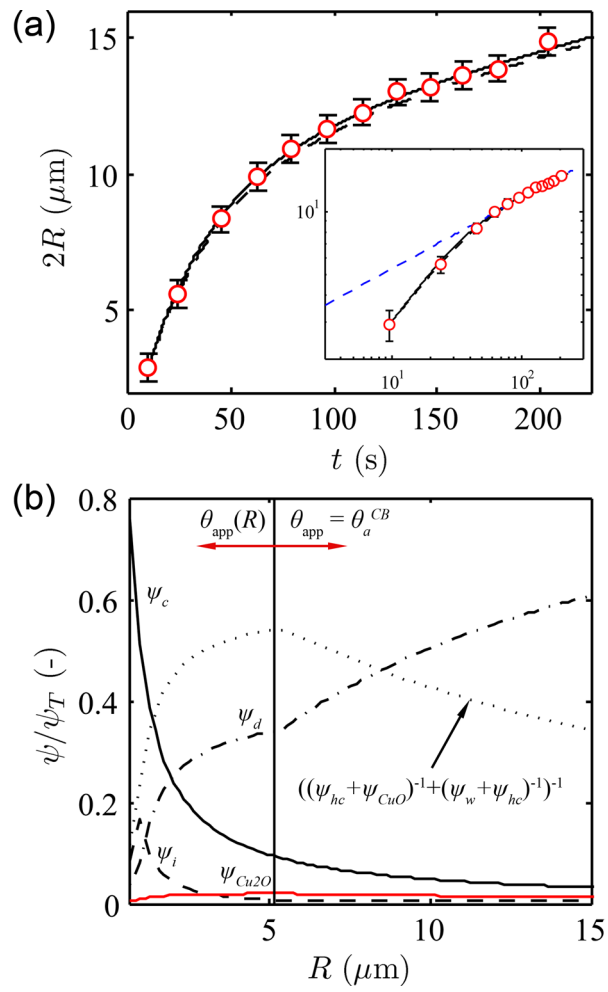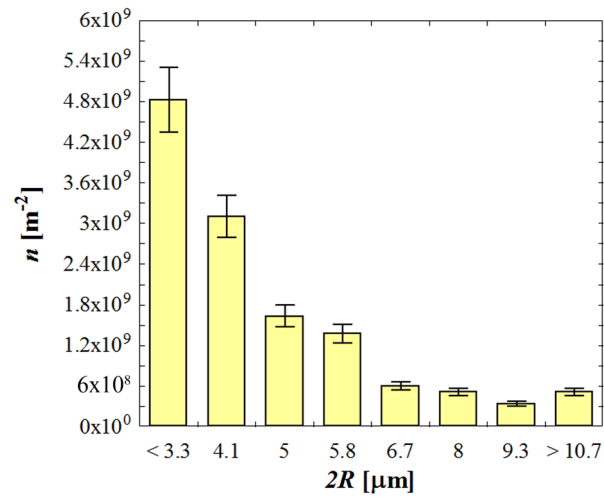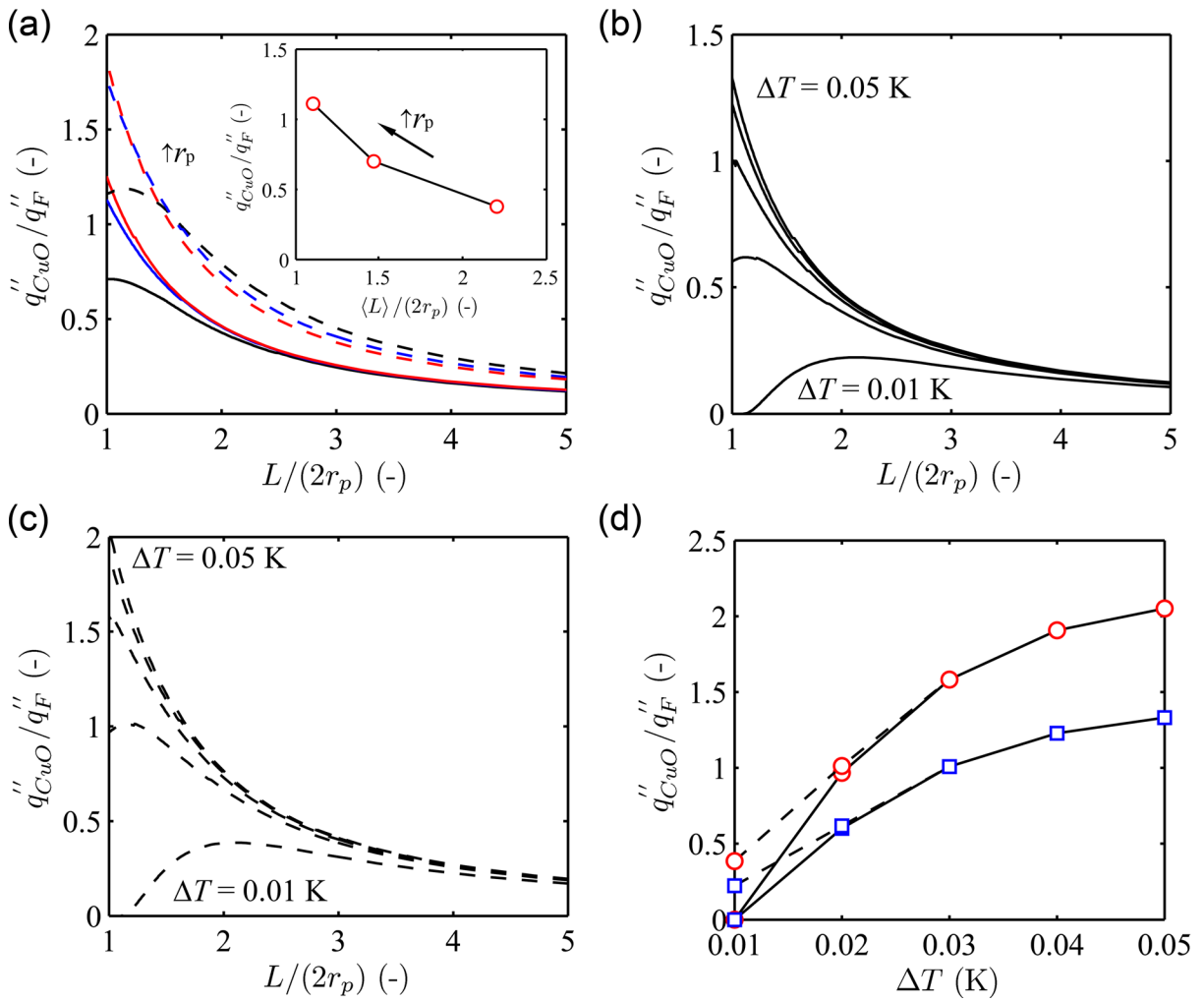
(a)

x (a.u.)

y (a.u.)

(b)

P (-)

$2L\sqrt{N}$ (-)
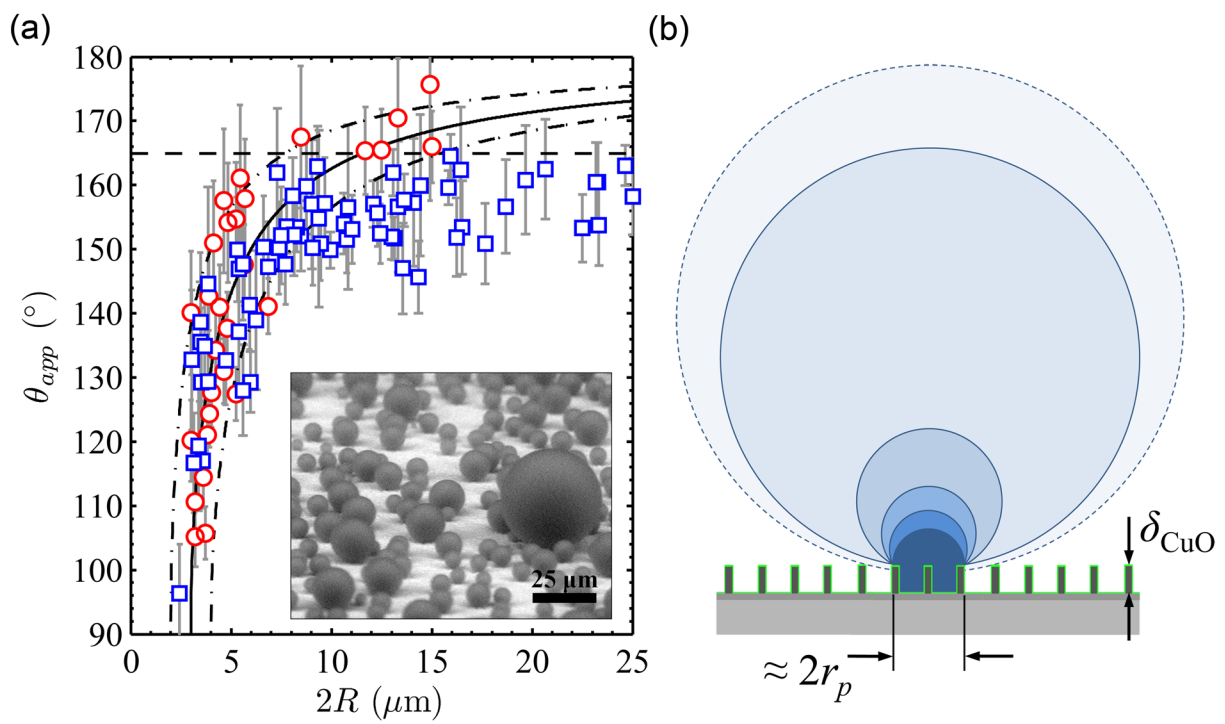
Fig_5.tif

Fig_6.tif

Fig_7.tif

Fig_8.tif

Fig_9.tif

Fig_10.tif